Behaviors of Si, B, Al, and Na during electrochemical reduction of borosilicate glass in molten CaCl

Katasho, Yumi; Yasuda, Kouji; Nohira, Toshiyuki

EDITORS' CHOICE

Behaviors of Si, B, Al, and Na during Electrochemical Reduction of Borosilicate Glass in Molten $CaCl_2$

Yumi Katasho,[a] Kouji Yasuda,[b,c,*] and Toshiyuki Nohira[a,*,z]

[a]*Institute of Advanced Energy, Kyoto University, Gokasho, Uji, Kyoto 611-0011, Japan*
[b]*Agency for Health, Safety and Environment, Kyoto University, Yoshida-hommachi, Sakyo-ku, Kyoto 606-8501, Japan*
[c]*Department of Fundamental Energy Science, Graduate School of Energy Science, Kyoto University, Yoshida-hommachi, Sakyo-ku, Kyoto 606-8501, Japan*

The electrochemical reduction of borosilicate glass in molten $CaCl_2$ at 1123 K was investigated. The behaviors of the constituent elements, i.e., Si, B, Al, Na, and K, were estimated using potential–pO^{2-} diagrams constructed from the thermodynamic data for the species. The diagrams suggested that the first cathodic wave in the cyclic voltammogram results from the reduction of the B_2O_3 component. The dissolution of the Na_2O and K_2O components, which was predicted from the diagrams, was confirmed by energy dispersive X-ray analysis of a borosilicate glass plate after immersion into molten $CaCl_2$ without electrolysis. The scanning electron microscopy/wavelength dispersive X-ray mappings and Raman spectrum for borosilicate glass reduced at 0.9 V vs. Ca^{2+}/Ca indicated that SiO_2 and B_2O_3 are reduced to Si and B–Si compound. The formation of Ca–Al–O compounds owing to the increase of O^{2-} ions is suggested. The pO^{2-} range during electrolysis at 0.9 V was indicated to be 2.95–3.46.

Manuscript received May 9, 2017. Published May 31, 2017.

In 2015, more than 11% of global electricity was produced by nuclear power plants.[1] Indeed, nuclear power generation is expected to replace conventional fossil-fuel-based thermal power generation in order to accommodate the energy demands of the growing global population. Considering the controls on carbon dioxide emissions, nuclear energy is attractive as a low-carbon-emission power source. However, the disposal of radioactive waste is a serious problem for nuclear power generation, especially in countries frequently hit by volcanic tremors and earthquakes, such as Japan, where the selection of sites suitable for the geological disposal of radioactive wastes is very difficult. Therefore, the development of an alternative to geological disposal is required.

In Japan, a new process for the disposal of radioactive wastes has been proposed.[2] In the first step of this process, long-lived fission products (LLFPs) such as ^{135}Cs, ^{79}Se, ^{93}Zr, and ^{107}Pd are separately recovered from high-level nuclear waste. They are then disposed as stable waste after their conversion by nuclear transmutation into short-lived or stable nuclides. If this process is established as a new disposal process for nuclear wastes, the amount of nuclear waste will be significantly reduced. This process has another potential advantage in that it may be used to recover valuable elements like platinum group metals, which can then be utilized for automobiles and fuel-cell catalysts. Moreover, if this process is realized, it is also applicable to the LLFPs already present in the large amount of existing vitrified waste. However, to accomplish this, each LLFPs must first be recovered from the vitrified waste.

Recently, the authors proposed a new method to recover LLFPs from vitrified wastes by electrochemical reduction in molten $CaCl_2$.[3]

$$MO_x + 2xe^- \rightarrow M + xO^{2-} \quad [1]$$

The three-dimensional (3-D) network structure of the glass (Si–O) is electrochemically destroyed. The reduction product is then subjected to the separation of each element. This process is superior to the conventional wet process using HF acid owing to its high processing rate and the relatively small amount of secondary radioactive waste produced.

In our previous study, the electrochemical reduction of borosilicate glass, which is composed of SiO_2, B_2O_3, Al_2O_3, Na_2O, and K_2O, was used as a model for real vitrified wastes (43–53 wt% SiO_2, 7–17 wt% B_2O_3, 3–5 wt% Al_2O_3, 6–24 wt% Na_2O, and $\leqq$25–35 wt% nuclear wastes[4]). The main component, i.e., SiO_2, was reduced to crystalline Si after potentiostatic electrolysis at 0.9 V vs. Ca^{2+}/Ca for 30 min. The formation of calcium aluminates was confirmed, while no reduction of Al_2O_3 was indicated. In addition, the reduction of B_2O_3 and the dissolution of Na_2O were suggested.

The construction of a potential–pO^{2-} diagram is a useful and important method to estimate the oxidation state and chemical form of elements in O^{2-} ion containing melts. Littlewood first introduced the concept of potential–pO^{2-} diagrams for electrowinning processes.[5] The diagrams are constructed by plotting the equilibrium potentials for the associated species against the negative logarithm of the activity of O^{2-} ions in the melt, $a_{O^{2-}}$.

$$pO^{2-} = -\log a_{O^{2-}} \quad [2]$$

Since then, potential–pO^{2-} diagrams have been constructed to help understand the chemical and electrochemical behaviors of many systems.[6–20] As examples for $CaCl_2$-based systems, Dring et al. prepared potential–pO^{2-} diagrams for the Ti–Ca–O–Cl system in molten $CaCl_2$ at 1173 K,[6–8] and we have reported the diagram for the Si–Ca–O–Cl system in $CaCl_2$ at 1123 K.[9] The potential–pO^{2-} diagrams for Al systems in molten NaCl–$CaCl_2$ and LiCl–$CaCl_2$ at 973 and 1173 K have been reported by Yan and Fray.[10] Furthermore, potential–pO^{2-} diagrams have also been constructed for LiCl–KCl,[11–16] NaCl–$CaCl_2$,[17,18] and other systems.[19,20]

In this study, we investigated the behavior of each constituent element during the electrochemical reduction of borosilicate glass in molten $CaCl_2$ at 1123 K. Firstly, potential–pO^{2-} diagrams were drawn from the thermodynamic data to evaluate the stable chemical species in the system. Secondly, immersed (but not reduced) borosilicate glass samples were characterized by scanning electron microscopy/energy dispersive X-ray (SEM/EDX) analysis. Finally, the electrochemically reduced samples were analyzed by SEM/EDX, scanning electron microscopy/wavelength dispersive X-ray (SEM/WDX) analysis, and Raman spectroscopy. The reaction mechanism was discussed with reference to the thermodynamic and experimental data.

Experimental

First, 500 g of $CaCl_2$ (> 95.0%, Wako Pure Chemical Industries, Ltd.) was crushed in an open dry chamber (HRW-60AR, Daikin Co. Ltd.) and placed in an alumina crucible (purity 99%, o.d. 90 mm, height 140 mm, As One Corp.). It was then dried at 453 K in a vacuum oven for more than 72 h. The crucible containing $CaCl_2$ was

*Electrochemical Society Member.
[z]E-mail: nohira.toshiyuki.8r@kyoto-u.ac.jp

transferred to a quartz glass vessel, and placed under vacuum at 773 K for 24 h to further remove the moisture. The subsequent experiments were conducted inside the quartz glass vessel at 1123 K under a dry Ar atmosphere.

Electrochemical measurements and potentiostatic electrolysis were conducted with a three-electrode method using an electrochemical measurement system (HZ-3000, Hokuto Denko Corp.). Glass-seal electrodes and wire-wound electrodes were used as the working electrodes. In the glass-seal electrodes, a tungsten rod (>99.95%, diameter: 2.0 mm, Nilaco corp.) was sealed in a borosilicate glass tube (Pyrex, SiO_2 80.8 wt%, B_2O_3 12.5 wt%, Al_2O_3 2.3 wt%, Na_2O 4.0 wt%, K_2O 0.4 wt%, o.d. 8 mm).[3] In the wire-wound electrodes, a borosilicate glass plate (Tempax, SiO_2 81 wt%, B_2O_3 13 wt%, Al_2O_3 2 wt%, Na_2O 3.3 wt%, K_2O 0.7 wt%, 5 mm × 15 mm × 1.1 mm) was wound with a Mo wire (>99.95%, diameter 0.2 mm, Nilaco Corp.).[3] The counter electrode was a graphite square rod (4 mm × 4 mm × 50 mm, IG-110, Toyo Tanso Co., Ltd.) and the reference electrode was an Ag^+/Ag electrode.[9] The chemical reaction between borosilicate glass and $CaCl_2$ at 1123 K was studied by immersing the wire-wound electrode in $CaCl_2$ for 30 minutes. A chromel-alumel thermocouple was used for temperature control.

The samples prepared by potentiostatic electrolysis or immersion were rinsed with distilled water to remove the residual salts and dried at room temperature. The glass-sealed electrodes were cut by a diamond cutter into ca. 5 mm long sections. For the wire-wound electrodes, the Mo wire was cut and removed from the plate carefully. The samples were observed using optical digital microscopy (Dino Lite PRO Polarizer DILITE30 AM-413ZT, Sanko Co., Ltd.) and SEM (VE-8800, Keyence Corp.). The compositions were analyzed by EDX (EDAX Genesis APEX2, AMETEK Co., Ltd.) at an accelerating voltage of 15 kV. After a sample was embedded in acrylic resin and polished, SEM/WDX spectroscopy (JXA-8530F, JEOL Ltd.) at an accelerating voltage of 10 kV was used for the cross-sectional mapping of elements. For Raman spectroscopy (Nano finder 30, wavelength: 532 nm, Tokyo Instruments Inc.), the samples were analyzed after they were rinsed with distilled water, 8% HCl aqueous solution, and 10% NaOH aqueous solution, successively.

Potential–pO^{2-} Diagrams in Molten $CaCl_2$ at 1123 K

Prior to the experiments, the potential–pO^{2-} diagrams were constructed for the related systems (M–Ca–O–Cl, where M = Si, B, Al, Na, or K in molten $CaCl_2$ at 1123 K). The thermodynamic data used for this study are listed in Tables I–VI.[9,21–36] The electrochemical window of $CaCl_2$ was calculated to be 3.26 V from the standard Gibbs energy of formation of $CaCl_2(l)$. The chemical potential of $CaO(l)$ was determined to be –496.9 kJ mol^{-1} from the solubility of CaO in molten $CaCl_2$ and the thermodynamic data for $CaO(s)$.[9] The evolution potential of 1 atm O_2 gas changes with pO^{2-} value, as indicated in Eq. 3.

$$E_{O_2/O^{2-}} = 2.575 + 0.111\,pO^{2-} \quad [3]$$

The frames of the potential–pO^{2-} diagrams for $CaCl_2$ at 1123 K are drawn by the dotted lines in Figures 1–4.

The Si–Ca–O–Cl system.—Figure 1a shows the potential–pO^{2-} diagram for the Si–Ca–O–Cl system in molten $CaCl_2$ at 1123 K. The diagram was drawn on the basis of the one reported in our previous paper,[9] but the thermodynamic data for Si–Ca alloys reported by Toba et al.,[24] were added. $CaSiO_3$ phase is found to be stable at $4.49 < pO^{2-} < 5.18$ in the melt. At positive potentials and high CaO concentrations (i.e., low pO^{2-} values), other calcium silicate compounds are stable. The potential at the three-phase boundary for $SiO_2/CaSiO_3/Si$ is calculated to be 1.32 V vs. Ca^{2+}/Ca, which has been reported to be the initial reduction potential of SiO_2.[9] Figure 1b shows the potential–pO^{2-} diagram in the low pO^{2-} and negative potential region, and indicates the formation of Si–Ca alloys. Five Si–Ca alloys are found at 1123 K. Since the equilibrium potential between Si and $CaSi_2$ is 0.50 V, the Si–Ca alloys form at a more negative potential.

The B–Ca–O–Cl system.—The potential–pO^{2-} diagram for the B–Ca–O–Cl system is shown in Figure 2. At $6.02 < pO^{2-} < 6.43$,

Table I. Thermochemical data for the M–O–Ca–Cl system at 1123 K.

Compound	Phase	Standard Gibbs energy of formation/ kJ mol^{-1}	References
$CaCl_2$	Liquid	−629.6	21
CaO	Solid	−517.4	21
CaO	Liquid	−496.9	9

Table II. Thermochemical data for the Si–Ca–O–Cl system at 1123 K.

Compound	Phase	Standard Gibbs energy of formation/ kJ mol^{-1}	References
SiO_2	Solid	−708.9	22
$SiCl_4$	Gas	−515.2	21, 23
$CaSi_2$	Solid	−97.1	24
Ca_3Si_4	Solid	−277.1	24
CaSi	Solid	−88.6	24
Ca_5Si_3	Solid	−358.3	24
Ca_2Si	Solid	−130.3	24
$CaSiO_3$	Solid	−1317.2	25, 26, 27
Ca_3SiO_5	Solid	−2432.1	28
$Ca_3Si_2O_7$	Solid	−3227.8	28

Table III. Thermochemical data for the B–Ca–O–Cl system at 1123 K.

Compound	Phase	Standard Gibbs energy of formation/ kJ mol^{-1}	References
B_2O_3	Liquid	−992.3	21, 25, 26
BCl_3	Gas	−346.2	21
CaB_6	Solid	−89.0	29
CaB_2O_4	Solid	−1623.0	21, 27, 30
CaB_4O_7	Solid	−2619.8	21, 27, 30
$Ca_2B_2O_5$	Solid	−2224.5	25, 26
$Ca_3B_2O_6$	Solid	−2798.7	25, 26

Table IV. Thermochemical data for the Al–Ca–O–Cl system at 1123 K.

Compound	Phase	Standard Gibbs energy of formation/ kJ mol^{-1}	References
Al_2O_3	Solid	−1320.2	31, 32
$AlCl_3$	Gas	−525.6	21
Al_2Ca	Solid	−65.1	33
$CaAl_2O_4$	Solid	−1879.1	22, 30, 34
$CaAl_4O_7$	Solid	−3211.7	21, 25, 26, 27
$Ca_3Al_2O_6$	Solid	−2926.0	25, 26, 27
$Ca_{12}Al_{14}O_{33}$	Solid	−15790.2	22

Table V. Thermochemical data for the Na–Ca–O–Cl system at 1123 K.

Compound	Phase	Standard Gibbs energy of formation / kJ mol^{-1}	References
Na_2O	Solid	−261.4	22
Na_2O_2	Liquid	−277.5	21, 35
NaCl	Liquid	−309.3	21, 25, 26, 36

Table VI. Thermochemical data for the K–Ca–O–Cl system at 1123 K.

Compound	Phase	Standard Gibbs energy of formation/ kJ mol^{-1}	References
K_2O	Liquid	−197.2	21, 23
K_2O_2	Liquid	−237.7	21, 23
KCl	Liquid	−326.2	25, 26

CaB_4O_7 phase is formed in the melt. The potential of 1.58 V at the three-phase boundary of B_2O_3/CaB_4O_7/B is more positive than the corresponding value for the Si–Ca–O–Cl system (1.32 V). The boundary between B_2O_3 or calcium borates and elemental B is more positive than that between SiO_2 or calcium silicates and elemental Si, as indicated with the red dashed line in Figure 2. Since the activity of $B_2O_3(l)$ is less than unity in the glass network, the stable region of B_2O_3 should be larger than that in Figure 2. The formation potential of CaB_6 from elemental B is 0.46 V. The calcium borates do not equilibrate with the CaB_6 phase because the elemental B phase is located between them (Figure 2). There is a discrepancy in the experimental report by Yin et al. in which CaB_6 was formed without elemental B during the reduction of CaB_2O_4 in $CaCl_2$ at 973 K.[37]

The Al–Ca–O–Cl system.—Figure 3a shows the potential–pO^{2-} diagram for the Al–Ca–O–Cl system. At $pO^{2-} = 3.46$, $CaAl_4O_7$ equilibrates with Al_2O_3. In the lower pO^{2-} region shown in Figure 3b, other calcium aluminates, $CaAl_2O_4$, $Ca_{12}Al_{14}O_{33}$, and $Ca_3Al_2O_6$, are stable depending on the conditions. Unlike the B–Ca–O–Cl system, the boundary between Al_2O_3 or calcium aluminates and Al metal is more negative than that between SiO_2 or calcium silicates and elemental Si, as indicated by the red dashed line in Figure 3a. The potential of 0.68 V at the three-phase boundary of Al_2O_3/$CaAl_4O_7$/Al is more negative than that for SiO_2/$CaSiO_3$/Si in the Si–Ca–O–Cl system (1.32 V). The formation potential of Al_2Ca alloy is found to be 0.36 V. In the potential–pO^{2-} diagram for Al–Ca–O–Cl in molten $CaCl_2$–NaCl reported by Yan et al.[10], the stable region of for Al_2Ca was larger than that in Figure 3a. We will report the details for the formation of Al–Ca alloy and the construction of the Al–Ca–O–Cl system in a separate paper.[38]

The Na–Ca–O–Cl and K–Ca–O–Cl systems.—The potential–pO^{2-} diagrams for the Na–Ca–O–Cl and K–Ca–O–Cl systems are shown in Figures 4a and 4b, respectively. The stable phases are NaCl(l) and Na(l) in Figure 4a and KCl(l) in Figure 4b. The dashed line in Figure 4b shows the formation potential of K(g) calculated from the decomposition voltage of KCl(l). The diagrams also suggest that both Na_2O and K_2O are thermodynamically favorable to dissolve in the melt.

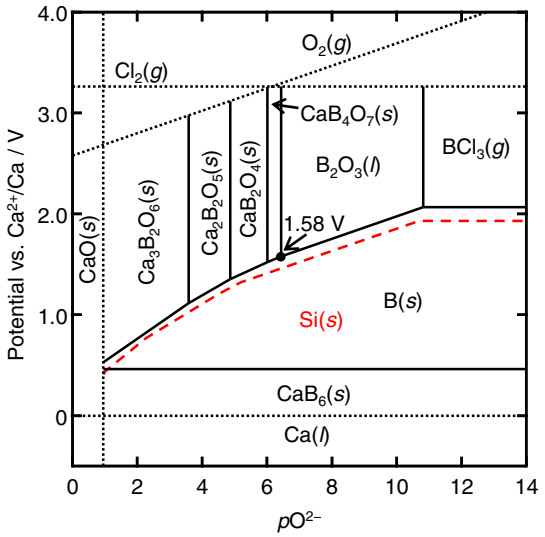

Figure 2. Potential–pO^{2-} diagram for the B–Ca–O–Cl system in molten $CaCl_2$ at 1123 K (red dashed line: boundary between Si and other compounds in the Si–Ca–O–Cl system).

$$Na_2O\,(s, in\ glass) + CaCl_2\,(l) \rightarrow 2\,NaCl\,(l) + CaO\,(l) \quad [4]$$

$$K_2O\,(s, in\ glass) + CaCl_2\,(l) \rightarrow 2\,KCl\,(l) + CaO\,(l) \quad [5]$$

Results and Discussion

The chemical reaction between the glass and molten $CaCl_2$.—Figure 5a-1 shows a photograph of the borosilicate glass plate after immersion in molten $CaCl_2$ for 30 min. A deformation of the glass plate is observed because Mo wire was wound in one fixed direction around the plate and the glass has a low softening point at around 1093 K.

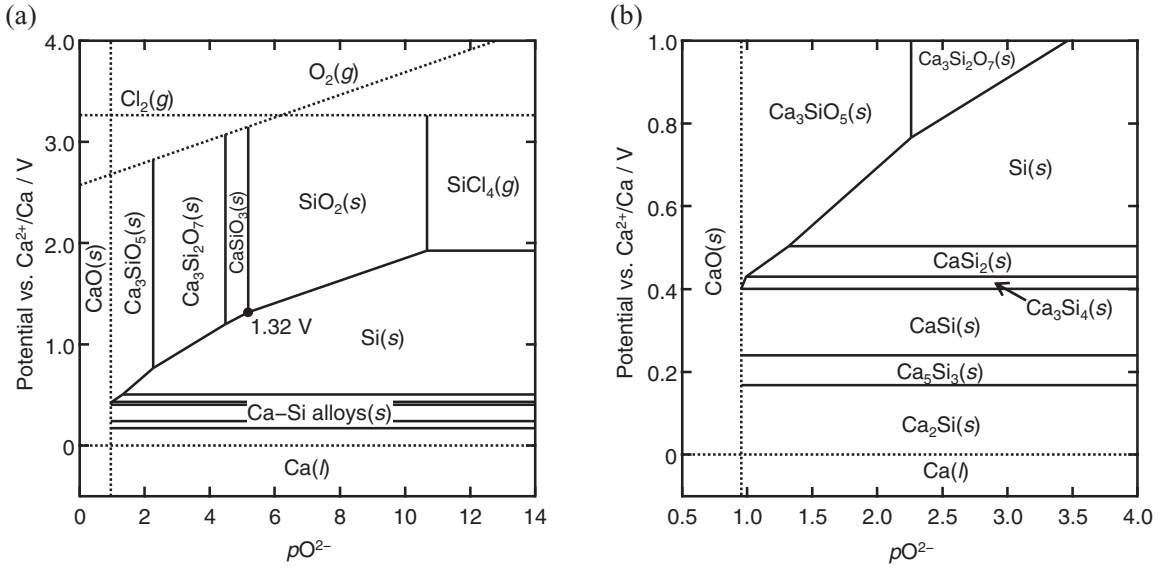

Figure 1. Potential–pO^{2-} diagrams for the Si–Ca–O–Cl system in molten $CaCl_2$ at 1123 K for the (a) whole region and (b) low pO^{2-} region.

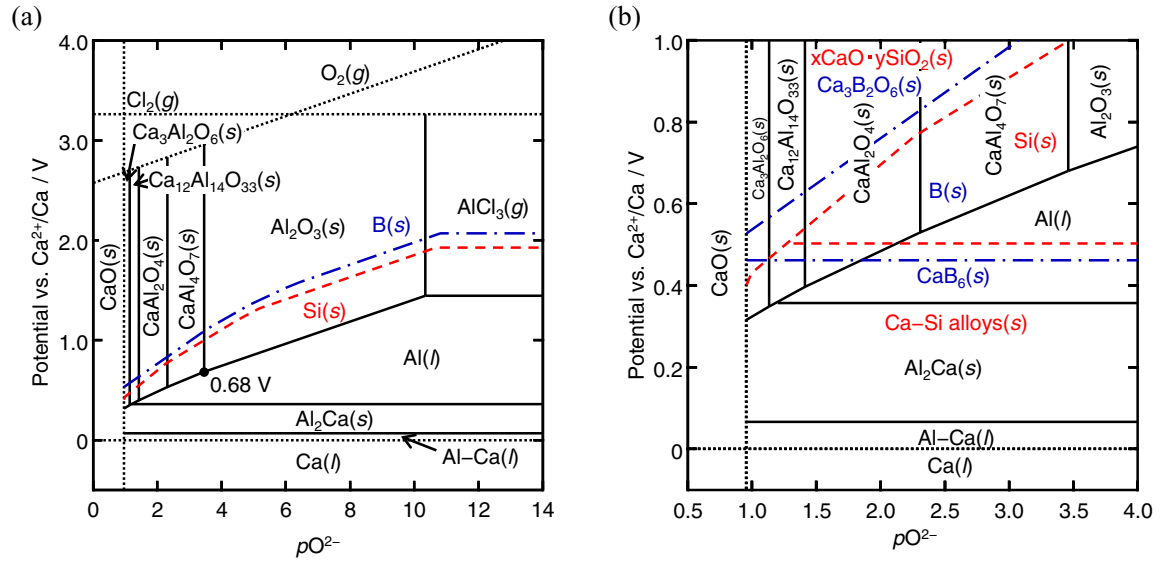

Figure 3. Potential–pO^{2-} diagrams for the Al–Ca–O–Cl system in molten $CaCl_2$ at 1123 K for the (a) whole region and (b) low pO^{2-} region (red dashed line: boundary between Si and other compounds in the Si–Ca–O–Cl system, blue dash-dot line: boundary between B and other compounds in the B–Ca–O–Cl system).

Furthermore, the devitrification of the plate, namely the color change from transparent to white, is observed. The devitrification suggests the occurrence of reactions between the glass surface and the melt. A surface SEM image and the EDX result are shown in Figure 5a-2 and 5a-3, respectively. The composition of the original plate is calculated from the composition ratio of each oxide in the borosilicate glass. The flake-like deposits of 1–5 μm in size in the dimples (point 1) are richer in Ca and Al compared with the original glass plate. Conversely, the porous surface (point 2) has areas with compositions similar to that of the original state, without the decrease of Na. The decrease of Na concentration is confirmed for both points 1 and 2. These behaviors suggest that the reaction of Na_2O with $CaCl_2$ results in the devitrification of the glass.

To confirm the progress of the chemical reaction into the inner bulk of the glass, a fractured section of the broken plate (Figure 5b-1) was observed by SEM/EDX (Figure 5b-2 and 5b-3). At point 3, the small holes in the porous phase have sizes of less than 1 μm. This porous phase has a similar composition to that of the original state, except for the decrease of Na. The porous phase has a similar morphology and composition to that of the porous phase observed by surface SEM at point 2. At point 4, the depth of the dimples near the flake-like deposits is around 10 μm, which agrees with the surface observation at point 2 in Figure 5a-2. The flake-like deposits (point 4) have a higher concentration of Ca and Al than that of the original glass, and a similar composition to that of the flake-like deposits at the surface (at point 1). At point 5, the fractured section has a smooth morphology at the micrometer scale. The composition is similar to that of the original state, and the concentration of Na is the same as that for the original composition. Therefore, it is concluded that the phase separation occurs only on the surface of the glass. The dissolution of Na_2O into the melt (Eq. 4) is also suggested by the potential–pO^{2-} diagram in Figure 4a. Although the behavior of K was not clarified due to the small K content, its oxide should also dissolve in the melt (Eq. 5) according to Figure 4b.

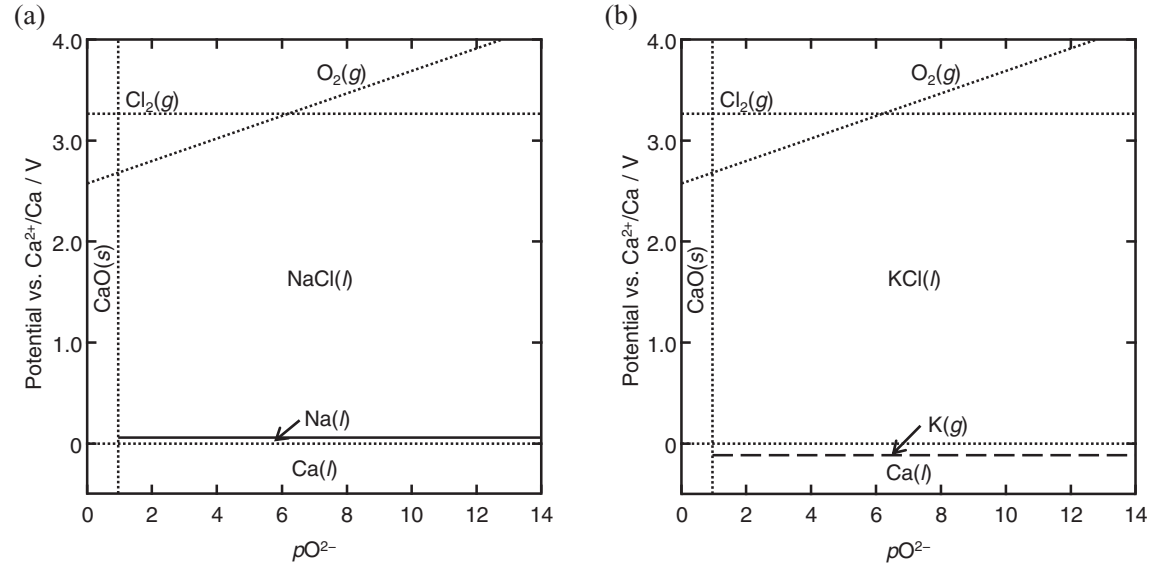

Figure 4. Potential–pO^{2-} diagrams for (a) the Na–Ca–O–Cl system and (b) the K–Ca–O–Cl system in molten $CaCl_2$ at 1123 K.

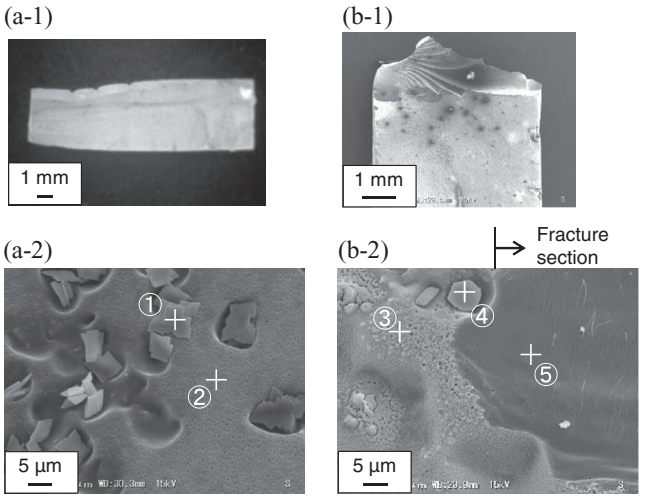

(a-3)

Element	Composition / At%		
	Original	Point ①	Point ②
Si	39.7	21.8	27.5
O	56.6	63.3	68.3
Al	1.1	10.1	2.4
Na	2.6	0.3	0.9
Ca	0.0	4.0	0.7
Cl	0.0	0.4	0.2

(b-3)

Element	Composition / At%		
	Point ③	Point ④	Point ⑤
Si	29.0	23.2	32.5
O	66.3	55.9	61.5
Al	1.8	13.6	2.3
Na	0.6	0.6	2.8
Ca	2.0	6.8	0.6
Cl	0.3	ND	0.4

Figure 5. (a-1) A microscope image, (a-2) SEM image, and (a-3) EDX analysis result for a borosilicate glass plate soaked in molten $CaCl_2$ for 30 min at 1123 K and rinsed in distilled water. SEM images in (b-1) low and (b-2) high magnification, and (b-3) EDX analysis result from a fractured surface obtained by breaking the plate after immersion shown in (a-1).

Considering the technique for the chemical strengthening of glass by ion exchange in molten salts,[39] the present results are reasonable. In the ion exchange process at temperature above the strain point, smaller ions are introduced to replace larger ones. For example, a soda-lime-silica glass soaked in a lithium-containing bath is strengthened by the exchange of Li^+ with Na^+ (ion radius: $Na^+ > Li^+$).[40] In the present study, the strain points for Pyrex and Tempax glass (783 and 791 K, respectively) are lower than 1123 K, and therefore the Ca^{2+} ions replace Na^+ ions (ion radius: $Na^+ > Ca^{2+}$).

For phase separation, the mechanism is explained as follows: The dissolution of Na_2O into the molten $CaCl_2$ results in an increase of the concentration of O^{2-} ions around the glass surface. According to the report, the higher content of CaO promotes the phase separation of SiO_2–CaO–Al_2O_3 glass into a (CaO–Al_2O_3)-rich phase and a SiO_2-rich phase at 1173 K.[41] Thus, Ca and Al rich flake-like deposits and porous phase are observed only on the glass surface after immersion in molten $CaCl_2$.

Cyclic voltammetry.—Figure 6 shows the cyclic voltammograms for a borosilicate glass sealed electrode.[3] The current in the 5th cycle is larger than that in the 1st cycle, which is explained by the increase of the reacting zone during the cyclic voltammetry measurement. In the negative scan, the cathodic current starts at 1.8 V. From the potential–pO^{2-} diagrams for Si–Ca–O–Cl and B–Ca–O–Cl (Figures 1a and 2a), the reduction of B_2O_3 is suggested to occur at more positive potentials than that of SiO_2 in the whole range of pO^{2-} values. Thus, the cathodic current at 1.8 V is attributed to the reduction of B_2O_3.

$$B_2O_3\,(s, in\ glass) + 6\,e^- \rightarrow 2\,B + 3\,O^{2-} \qquad [6]$$

A large cathodic current flows from 1.3 V, which corresponds to the reduction of SiO_2 to Si.[3] The large current is due to the large

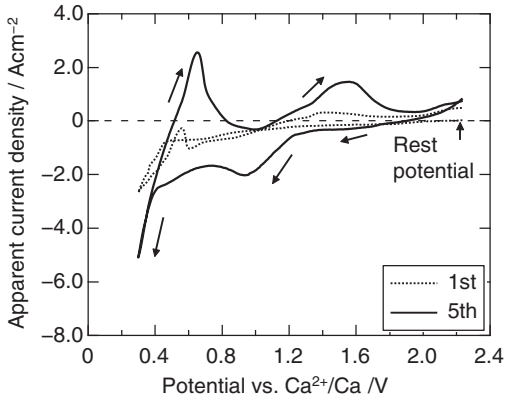

Figure 6. Cyclic voltammograms for borosilicate glass sealed electrodes in molten $CaCl_2$ at 1123 K. Scan rate: 100 mV s^{-1}. (Ref. 3)

composition ratio of SiO_2 in the glass.

$$SiO_2\,(s, in\ glass) + 4\,e^- \rightarrow Si + 2\,O^{2-} \qquad [7]$$

A sharp increase of cathodic current is observed at 0.4 V, which can be explained by the formation of Si–Ca alloys.[3,24,42]

$$Si + Ca^{2+} + 2\,e^- \rightarrow Si\text{–}Ca \qquad [8]$$

After the switching potential at 0.3 V, an anodic current peak is observed at 0.65 V for dissolution of Ca from the Si–Ca alloy. Another anodic current peak at 1.5 V correspond to the oxidation of Si to SiO_2. A small anodic current observed from 1.8 V is likely due to the oxidation of B to B_2O_3.

Characterization of the reduction product prepared by potentiostatic electrolysis.—The wire-wound borosilicate glass electrodes were potentiostatically electrolyzed to investigate its reduction behavior at different potentials (0.6, 0.9, and 1.4 V). A larger current is observed at more negative potential (Figure 7a). As seen in Figure 7b, the plate color changes from colorless to brown at 0.6 and 0.9 V, while no change is observed for 1.4 V. The area of color change is larger at 0.6 V than at 0.9 V. At 1.4 V, bubbles are formed in the glass at the contact points with the Mo wire. Bubbles are also observed in the borosilicate glass at 0.9 and 0.6 V.

The bubbles in the glass are thought to be formed by H_2 gas generated from water reduction in the glass. There is a report that silanols (≡Si–OH) remain both on the surface and inside the silica (SiO_2) at 1123 K, and H_2O is generated by the reaction in Eq. 9 when the temperature increases.[43]

$$2\ \text{–OH}\,(in\ glass) \rightarrow 2\ \text{–O–} + H_2O \qquad [9]$$

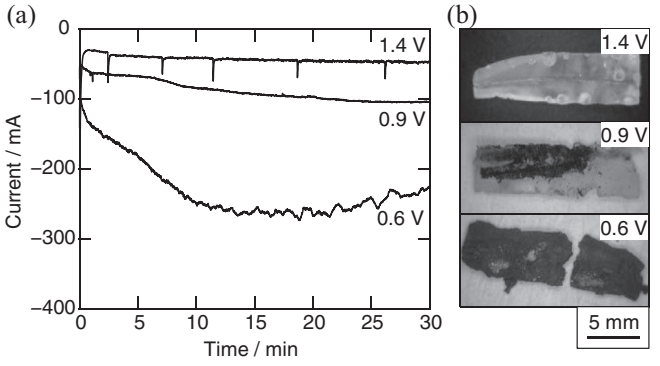

Figure 7. (a) Current-time curves during the reduction of wire-wound borosilicate glass electrodes at 0.6, 0.9, and 1.4 V vs. Ca^{2+}/Ca for 30 min in $CaCl_2$ at 1123 K and (b) microscope images of the obtained samples prepared by the electrolysis.

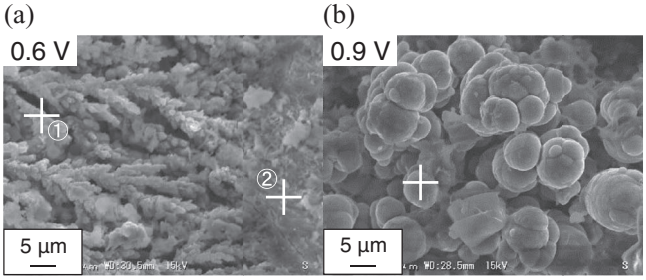

(c)

Element	Composition / At%		
	(a)-①	(a)-②	(b)
Si	73.2	20.0	86.3
O	17.9	62.6	4.2
Al	1.8	0.8	2.7
Na	0.9	0.3	ND
Ca	3.0	13.5	5.8
Cl	3.3	2.7	1.0

Figure 8. SEM images of reduction products obtained by the electrochemical reduction of a borosilicate glass plate at (a) 0.6 and (b) 0.9 V vs. Ca^{2+}/Ca for 30 min. (c) EDX analysis results for each sample.

$$2\,H_2O\,(in\ glass) + 4\,e^- \rightarrow 2\,O^{2-} + 2\,H_2(g) \qquad [10]$$

If these reactions occur, H_2 gas is generated near the contact point between the Mo wire and the surface of the glass. These bubbles are not observed for the silica glass plate at 1.4, 0.9, and 0.6 V.[42] The difference in the behaviors of borosilicate glass and silica glass is also likely due to the softening points (SiO_2: 1773 K, Tempax glass: 1093 K). In the case of borosilicate glass, H_2 gas can deform the glass because of the low softening point, allowing bubbles to form at the contact points with the Mo wire.

Behaviors of Si and Na.—The formation of Si has been previously confirmed by XRD analysis of the reduction products for borosilicate glass prepared at 0.6 and 0.9 V.[3] The results of the SEM observation and EDX analysis of the reduction products of borosilicate glass at 0.6 and 0.9 V (Figure 8) indicate the reduction of SiO_2 to Si. The formation of connected granular products with a high concentration of Si is observed at both potentials. The size of the grains is smaller at 0.6 than that at 0.9 V. The largest diameter of the grains is ca. 1 μm at 0.6 V and ca. 10 μm at 0.9 V. At 0.6 V (Figure 8a), the connected granular products grow from regions of high Si and low O concentrations (point 1) toward regions of high O concentration (point 2).

The dissolution of Na_2O into molten $CaCl_2$ during the electrochemical reduction was confirmed by SEM/EDX analysis for both 0.6 and 0.9 V. The concentrations of Na for all three points in Figure 8 are lower than the initial Na concentration of the plate (2.6 at%). These results agree with the reaction between borosilicate glass and molten $CaCl_2$ in the immersion experiment, as discussed in the chemical reaction between the glass and molten $CaCl_2$ section.

Behavior of B.—To investigate the reduction behavior of B, Raman spectroscopy was conducted for the borosilicate glass reduced at 0.9 V for 30 min in $CaCl_2$, as shown in Figure 9. For reference, the spectrum of a p-type single crystal silicon wafer was also measured. In addition to the peak for crystalline Si (520 cm^{-1}), a small peak at 618 cm^{-1} appears for the reduced borosilicate glass. The peak position agrees well with the reported values for ^{11}B–Si (620 cm^{-1}) in B-doped bulk silicon[44] and ^{11}B–Si (618 cm^{-1}) in B-doped Si-nanowire.[45] In this study, we used natural boron (^{11}B: 80.2%, ^{10}B: 19.8%) and the more abundant ^{11}B–Si peak was detected. Therefore, the reduction of B_2O_3 in the borosilicate glass, which was suggested by the cyclic voltammetry and potential–pO^{2-} diagram, is confirmed. The reduced products have B–Si bonds in a B-containing crystalline Si phase.

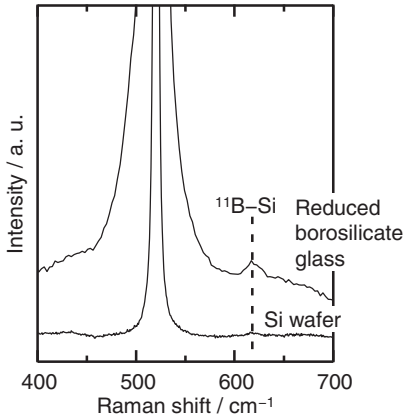

Figure 9. Raman spectra for the borosilicate glass reduced at 0.9 V vs. Ca^{2+}/Ca for 30 min in $CaCl_2$ and p-type single crystal silicon wafer. A 532 nm-excitation laser was used.

Behavior of Al.—The reduction behavior of Al_2O_3 was investigated by SEM/WDX cross-sectional mappings of the products obtained at 0.9 V for 30 min (Figure 10). The result agrees well with previously reported surface SEM/EDX mappings where most of the O-rich areas coincide with the Al-rich areas and Ca-rich areas.[3] This result indicates that Al_2O_3 is not reduced and that calcium aluminates are formed both in the bulk and on the surface of the reduced products. In the potential–pO^{2-} diagram for the Al–Ca–O–Cl system (Figure 3), the conditions for no reduction of Al_2O_3 and the formation of calcium aluminates is found to be the region where $pO^{2-} < 3.46$.

Interpretations of the behavior of each element.—Figure 10 shows that several regions inside the granules produced contain Si, Al, Ca, and O (one such region is shown as a white circle in Figure 10). This result is interpreted as being due to a mixture of reduced silicon and unreduced calcium aluminates, which agrees with the previous discussions.

The reaction conditions including the pO^{2-} value can be deduced from the experimental results. Figure 11a shows the superimposed potential–pO^{2-} diagrams for the Si–Ca–O–Cl, B–Ca–O–Cl, and

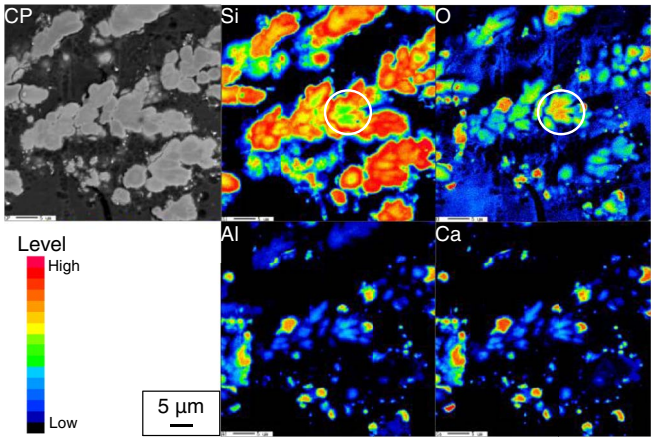

Figure 10. SEM/WDX cross-sectional maps of products obtained by the electrochemical reduction of a sealed borosilicate glass electrode at 0.9 vs. Ca^{2+}/Ca for 30 min in molten $CaCl_2$ (White circle shows the inside of the grains containing Si, Al, Ca, and O).

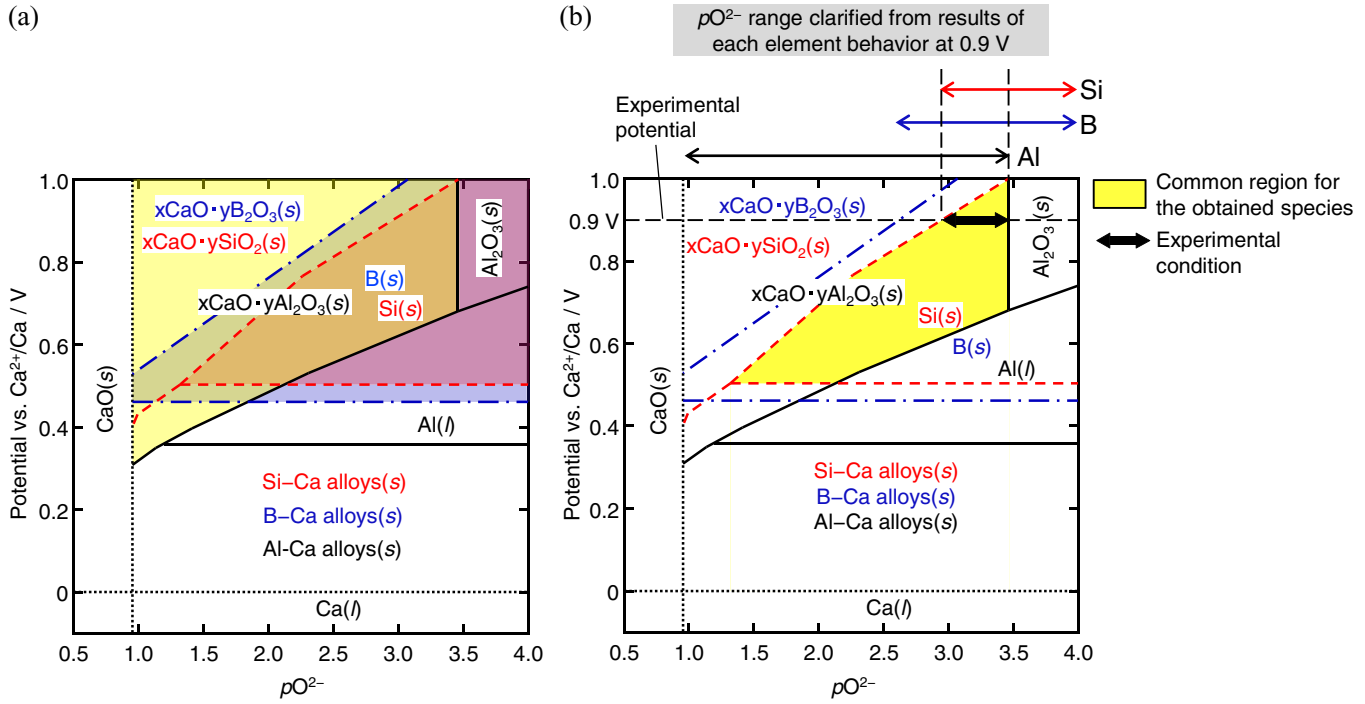

Figure 11. Superimposed potential–pO^{2-} diagrams for the Si–, B–, and Al–Ca–O–Cl systems in molten $CaCl_2$ at 1123 K for the low pO^{2-} region (red dashed line: boundary between Si and other compounds in the Si–Ca–O–Cl system, blue dash-dot line: boundary between B and other compounds in the B–Ca–O–Cl system, black line: boundary between Al and other compounds in the Al–Ca–O–Cl system). (a) The stable region for Si, B, and calcium aluminates. (b) Common region for the obtained species and pO^{2-} range obtained from experimental results for each element behavior at 0.9 V.

Al–Ca–O–Cl systems. In this diagram, the common region stable for calcium aluminates (yellow), Si (red), and B (blue) exists. The common region for the obtained species is shown in yellow in Figure 11b. At 0.9 V, the pO^{2-} values for the formation of Si and B are larger than 2.95 and 2.62, respectively. For the formation of calcium aluminates, the pO^{2-} value is smaller than 3.46. To summarize, the reduction product in this study was formed in the range $2.95 < pO^{2-} < 3.46$. This pO^{2-} range is smaller than the reported pO^{2-} value of 5.5 for the electrochemical reduction of SiO_2 in molten $CaCl_2$.[9] One of the reasons for the decreased pO^{2-} value is the emission of O^{2-} ions by the dissolution of Na_2O. Although calcium silicates are formed by the reaction with CaO in the melt as an intermediate in the reduction of SiO_2,[9] they are then reduced to Si to produce O^{2-} ions at 0.9 V. B_2O_3 will have a similar reduction pathway to that of SiO_2. Conversely, calcium aluminates are not reduced in this pO^{2-} range, and the CaO formed both by the dissolution of Na_2O and the reduction of SiO_2 and B_2O_3 will react with Al_2O_3. Therefore, the value of pO^{2-} remains around 3.46 where the boundary between $CaAl_4O_7$ and Al_2O_3 exists.

Based on the results obtained throughout this study, including the potential–pO^{2-} diagrams and characterizations of the products, the reaction mechanism and the behavior of each element during the reduction of borosilicate glass at 0.9 V are summarized as follows:

1. Dissolution of Na_2O and K_2O and emission of O^{2-} ions.
2. Phase separation of borosilicate glass.
3. Reduction of SiO_2 to Si via a $Ca_xSi_yO_z$ intermediate and B_2O_3 to B via a $Ca_xB_yO_z$ intermediate at 0.9 V.
4. Reaction of the more abundant O^{2-} ions with Al_2O_3 to form calcium aluminates.
5. Repetition of steps 1–4 leading to a pO^{2-} range of $2.95 < pO^{2-} < 3.46$.

Conclusions

The electrochemical reduction behavior of borosilicate glass with a composition of 80.8 wt% SiO_2, 12.5 wt% B_2O_3, 2.3 wt% Al_2O_3, 4.0 wt% Na_2O, and 0.4 wt% K_2O was investigated in molten $CaCl_2$ at 1123 K. SiO_2 was confirmed to be reduced to Si both at 0.6 and 0.9 V. Raman spectroscopy revealed the reduction of B_2O_3 at 0.9 V to form B–Si bonds in a B-containing crystalline Si phase. Na_2O was dissolved only by immersion into molten $CaCl_2$, which was confirmed by EDX analysis. As for Al_2O_3, the formation of calcium aluminates without reduction was confirmed at 0.9 V by SEM/WDX mapping. The above results agree with the potential–pO^{2-} diagrams constructed from published thermodynamic data. The pO^{2-} range was indicated to stay at $2.95 < pO^{2-} < 3.46$ during the electrolysis at 0.9 V as a result of the dissolution of Na_2O, the reduction of B_2O_3 and SiO_2, and the formation of calcium aluminates.

Acknowledgments

This work was partly funded by the ImPACT Program of the Council for Science, Technology, and Innovation (Cabinet Office, Government of Japan).

References

1. OECD/IEA, *Key World Energy Statistics 2016*, https://www.iea.org/publications/freepublications/publication/KeyWorld2016.pdf,
2. *Impulsing Paradigm Change through Disruptive Technologies Program. Reduction and Resource Recycle of High Level Radioactive Wastes with Nuclear Transmutation.* http://www.jst.go.jp/impact/en/program08.html.
3. Y. Katasho, X. Yang, K. Yasuda, and T. Nohira, *J. Electrochem. Soc.*, **163**, D622 (2016).
4. M. I. Ojovan and W. E. Lee, *Metall. Mater. Trans. A*, **42**, 837 (2011).
5. R. Littlewood, *J. Electrochem. Soc.*, **109**, 525 (1962).
6. K. Dring, R. Dashwood, and D. Inman, *J. Electrochem. Soc.*, **152**, D184 (2005).
7. K. Dring, R. Dashwood, and D. Inman, *J. Electrochem. Soc.*, **152**, E104 (2005).
8. K. Dring, R. Bhagat, M. Jackson, R. Dashwood, and D. Inman, *J. Alloys Compd.*, **419**, 103 (2006).
9. K. Yasuda, T. Nohira, R. Hagiwara, and Y. H. Ogata, *J. Electrochem. Soc.*, **154**, E95 (2007).
10. X. Y. Yan and D. J. Fray, *J. Appl. Electrochem.*, **39**, 1349 (2009).
11. G. Landresse and G. Duyckaerts, *Anal. Chim. Acta*, **73**, 121 (1974). (In French)

12. M. Takahashi, Y. Katsuyama, and Y. Kanzaki, *J. Electroanal. Chem. Interfacial Electrochem.*, **62**, 363 (1975).
13. R. Lysy and G. Duyckaerts, *Anal. Chim. Acta*, **96**, 125 (1978). (In French)
14. I. Uchida, J. Niikura, and S. Toshima, *J. Electroanal. Chem. Interfacial Electrochem.*, **124**, 165 (1981).
15. G. Picard, F. Seon, and B. Tremillon, *J. Electrochem. Soc.*, **129**, 1450 (1982).
16. Y. Katayama, R. Hagiwara, and Y. Ito, *J. Electrochem. Soc.*, **142**, 2174 (1995).
17. A. M. MartıÍnez, Y. Castrillejo, E. Barrado, G. M. Haarberg, and G. Picard, *J. Electroanal. Chem.*, **449**, 67 (1998).
18. D. Lambertin, J. Lacquement, S. Sanchez, and G. Picard, *Electrochem. Commun.*, **4**, 447 (2002).
19. H. Hayashi, S. Yoshizawa, and Y. Ito, *Electrochim. Acta*, **28**, 149 (1983).
20. Y. Ito, H. Hayashi, Y. Itoh, and S. Yoshizawa, *Bull. Chem. Soc. Jpn.*, **58**, 3172 (1985).
21. Landolt-Börnstein, *Thermodynamic Properties of Inorganic Material*, Scientific Group Thermodata Europe (SGTE), Springer-Verlag, Berlin-Heidelberg (1999).
22. I. Barin, *Thermochemical Data of Pure Substances*, VCH Verlags Gesellschaft, Weinheim (1989).
23. Glushko, *Thermocenter of the Russian Academy of Sciences*, Moscow, Russia (1994).
24. T. Toba, K. Yasuda, T. Nohira, X. Yang, R. Hagiwara, K. Ichitsubo, K. Masuda, and T. Homma, *Electrochemistry*, **81**, 559 (2013).
25. I. Barin, *Thermochemical Data of Pure Substances, Part I*, VCH Verlags Gesellschaft, Weinheim (1993).
26. I. Barin, *Thermochemical Data of Pure Substances, Part II*, VCH Verlags Gesellschaft, Weinheim (1993).
27. A. J. Bard, R. Parsons, and J. Jordan, *Standard Potentials in Aqueous Solution*, Marcel Dekker Inc., New York (1985).
28. L. B. Pankratz, *Thermodynamic Properties of Carbides, Nitrides, and Other Selected Substances.*, U.S. Dept. of the Interior, Washington, DC, pp. **957**, (1995).
29. A. V. Blinder, S. P. Goridienko, É. V. Marek, and V. B. Muratov, *Powder Metall. Met. Ceram.*, **36**, 409 (1997).
30. O. Knacke, O. Kubaschewski, and K. Hesselman, *Thermochemical Properties of Inorganic Substances*, 2nd ed., Springer-Verlag, Berlin (1991).
31. I. Barin, O. Knacke, and O. Kubaschewski, *Thermochemical properties of inorganic substances*, Supplement, Springer-Verlag, Berlin, 861 (1977).
32. I. Barin, O. Knacke, and O. Kubaschewski, *Thermodynamic Properties of Inorganic Substances*, Springer-Verlag, Berlin and New York, NY, 1973, Supplement (1977).
33. V. P. Itkin, C. B. Alcock, P. J. van Ekeren, and H. A. J. Oonk, *Bull. Alloy Phase Diagrams*, **9**, 652 (1988).
34. M. Binnewies and E. Milke, *Thermochemical Data of Elements and Compounds*, 2nd edition, Wiley-VCH, Weinheim (2002).
35. M. W. Chase, *JANAF Thermochemical Tables, 3rd ed., J. Phys. Chem. Ref. Data*, **14**, 1 (1985).
36. TC RAS Thermodynamic Database for Organic Compounds, (1986).
37. H. Yin, D. Tang, X. Mao, W. Xiao, and D. Wang, *J. Mater. Chem. A*, **3**, 15184 (2015).
38. H. Kadowaki, Y. Katasho, K. Yasuda, and T. Nohira, *J. Electrochem. Soc.*, to be submitted.
39. A. L. Zijlstra and A. J. Burggraaf, *J. Non. Cryst. Solids*, **1**, 49 (1968).
40. H. P. Hood and S. D. Stookey, U. S. Pat. 2779136 (1957).
41. T. Ohgaki, A. Higashida, K. Soga, and A. Yasumori, *J. Electrochem. Soc.*, **154**, J163 (2007).
42. K. Yasuda, T. Nohira, and Y. Ito, *J. Phys. Chem. Solids*, **66**, 443 (2005).
43. L. T. Zhuravlev and V. V. Potapov, *Russ. J. Phys. Chem.*, **80**, 1119 (2006).
44. C. P. Herrero and M. Stutzmann, *Phys. Rev. B*, **38**, 12668 (1988).
45. N. Fukata, *Adv. Mater.*, **21**, 2829 (2009).